Available online at www.sciencedirect.com
ScienceDirect
International Journal of Heat and Fluid Flow 28 (2007) 894–908
International Journal of HEAT AND FLUID FLOW
www.elsevier.com/locate/ijhff

Large-eddy simulation of three-dimensional flow around a hill-shaped obstruction with a zonal near-wall approximation

F. Tessicini, N. Li, M.A. Leschziner *

Department of Aeronautics, Imperial College London, Prince Consort Road, London, SW7 2AZ, UK

Received 24 July 2006; received in revised form 22 November 2006; accepted 22 January 2007
Available online 26 March 2007

Abstract

The focus of the paper is on the performance of an approximate 'zonal' near-wall treatment applied within a LES strategy to the simulation of flow separating from a three-dimensional hill at high Reynolds numbers. In the zonal scheme, the state of the near-wall layer of the flow is described by parabolized Navier–Stokes equations solved on a sub-grid embedded within a global LES mesh. The solution of the boundary-layer equations returns the wall shear stress to the LES domain as a wall boundary condition. Simulations are presented for grids containing between 1.5 and 9.6-million-nodes, the one on the finest grid being a pure LES. The comparisons included demonstrate that the zonal scheme provides a satisfactory representation of most flow properties, even on the coarsest grid, whereas the pure LES on the coarsest grid completely fails to capture the separation process.

Keywords: LES; Near-wall modelling; Zonal two-layer modelling

1. Introduction

Three-dimensional separation from curved surfaces frequently occurs in external aerodynamics, ship hydrodynamics, turbo-machinery and all manner of curved ducts, curved aero-engine intakes being one example. Unlike separation from a sharp edge, that from a curved surface is always characterised by a highly convoluted and patchy separation area, which moves rapidly in time and space as a consequence of upstream turbulence and Kelvin–Helmholtz instability provoked by the separation process. Separation may also be intermittent and even periodic, being associated with von-Karman vortex shedding and/or Taylor–Goertler vortices. Because the separation location is not fixed by a specific geometric feature – say, a sharp corner or edge – its characteristics depend sensitively on the outer flow and also the reattachment process, if occurring at all. In circumstances in which geometric three-dimensionality is relatively weak, a closed recirculation region may arise following separation. This is the case, for example, in a spanwise uniform, unswept cylinder or surface bump, which is confined in the spanwise direction by walls that are perpendicular to the cylinder or the bump. In more complex conditions, the surface of the body interacting with the flow will be highly three-dimensional, as is the case with highly-loaded swept wings and fan blades, strongly curved circular ducts and three-dimensional smooth (hill-shaped) constrictions in conduits. In such cases, the separation pattern tends to be much more convoluted, featuring, in the mean, a wide range of topological entities such as curved detachment and attachment lines and nodes, focal points and saddles (Perry and Chong, 1987; Helman and Hesselink, 1990). Large vortical structures are shed from the surface over a substantial surface area around the mean separation line. Hence, the turbulence is distinctly non-local, and its dynamics are important. The boundary layer approaching the separation region is subjected to strong skewing and normal straining, with consequent major changes to the turbulence structure. Finally, strong streamwise vorticity and associated flow curvature within and downstream of the separated region

* Corresponding author. Tel.: +44 207 594 5061; fax: +44 207 584 8120.
E-mail address: mike.leschziner@imperial.ac.uk (M.A. Leschziner).

0142-727X/$ - see front matter © 2007 Elsevier Inc. All rights reserved.
doi:10.1016/j.ijheatfluidflow.2007.01.006

provoke further complex interactions between the mean strain and the turbulence field.

A generic laboratory flow that combines all above features is that around a hill placed in a duct, as shown in Fig. 1. This flow has been examined extensively over several years by Simpson et al. (2002) and Byun and Simpson (2005), using elaborate LDV techniques, as well as HWA, and it is increasingly viewed as a key three-dimensional test case for prediction procedures. The hill is subjected to a boundary layer of thickness roughly one half of the hill height, one consequence of this thickness being that the structure of the boundary layer can be expected to be highly influential to the downstream evolution of the flow. The Reynolds number, based on hill height and free-stream velocity, is 130,000. As the boundary layer interacts with the hill, it is subjected to strong skewing prior to separation on the leeward side of the hill. The flow detaches, in the mean, along a separation line, roughly half-way between the hill crest and the hill foot. This merges into focal points on the leeward hill surface. Streamwise-oriented vortices are shed from the focal points, and these evolve alongside the legs of a strong horseshoe vortex formed at the upstream foot of the hill. Hugging the hill's leeward side is a closed thin recirculation region, which reattaches close to the leeward foot of the hill.

Attempts to compute this flow with RANS methods, whether undertaken in a steady or an unsteady mode, have not been successful. For example, Wang et al. (2004) report an extensive study with various non-linear eddy-viscosity and second-moment-closure models, all giving seriously excessive separation, insufficient rate of post-reattachment recovery and wrong flow structure downstream of the hill. Attempts to induce shedding-like behaviour, within the RANS framework, through the introduction of periodic excitation in the inlet flow, invariably led to a steady flow after the excitation ceased. Similarly unsuccessful RANS results were also reported by Persson et al. (2006) in a recent study. The defects noted above are not entirely surprising, as none of the models accounts for the dynamics of the large-scale, highly energetic motions unavoidably accompanying unsteady separation.

Large-eddy simulation naturally captures, at least in principle, the dynamics of the separation process. However, the simulation of wall-bounded flows at practical Reynolds numbers faces almost untenable resource challenges, because the near-wall grid density required for the near-wall structure to be resolved rises roughly in proportion to Re^2. When gross features of the resolved flow are substantially affected by near-wall shear and turbulence, as may be the case herein, the quality demands from the numerical mesh, in terms of density, skewness, cell aspect ratio and inter-nodal expansion ratio, are especially stringent and further increase the computational costs.

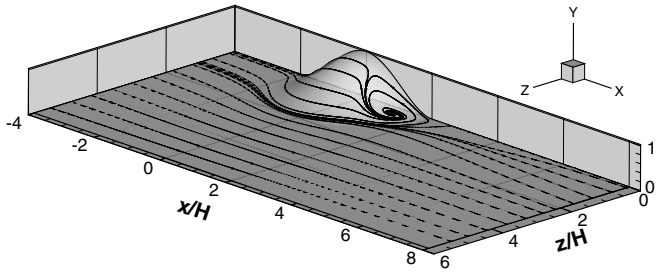

Fig. 1. Flow over a three-dimensional hill.

Approaches that aim to bypass the above exorbitant requirements are based either on wall functions or hybrid or zonal RANS-LES schemes. The use of equilibrium-flow wall functions goes back to early proposals by Deardorff (1970) and Schumann (1975), and a number of versions have subsequently been investigated, which are either designed to satisfy the logarithmic velocity law (referred to as 'log-law', henceforth) in the time-averaged field or, more frequently, involve an explicit log-law or closely related power-law prescription of the instantaneous near-wall velocity (e.g. Werner and Wengle, 1991; Hoffmann and Benocci, 1995; Temmerman et al., 2002). These can provide useful approximations in conditions not far from equilibrium, but cannot be expected to give a faithful representation of the near-wall layer in separated flow. The alternative of adopting a RANS-type turbulence-model solution for the inner near-wall layer is assumed to offer a more realistic representation of the near-wall flow in complex flow conditions at cell-aspect ratios much higher than those demanded by wall-resolved simulations.

The best-known realization of the combined RANS-LES concept is Spalart et al.'s (1997) DES method. This is one of a class of 'seamless' methods, the most elaborate forms of which being based on a spectral RANS-LES partitioning (Schiestel and Dejoan, 2005; Chaouat and Schiestel, 2005). The DES scheme is designed to return a RANS solution in attached flow regions and revert to LES once separation is predicted. This is done by arranging the wall-parallel cell dimensions Δx and/or Δz to be much larger than the wall-normal distance Δy, the consequence being an outward shift of the RANS-LES switching position $y_{\text{int}} = \min(y_{\text{wall}},\ C_{\text{DES}} \times \max(\Delta x,\Delta y,\Delta z))$ away from the wall and a dominance of the RANS scheme. This concept of extensive steady patches co-existing, seamlessly, with unsteady resolved portions raises important question marks against physical realism in areas in which separated regions border boundary layers and in post-reattachment recovery. Also, in general flows, the streamwise grid density often needs to be high to achieve adequate resolution of complex geometric and flow features, both close to the wall (e.g. in separation and reattachment) and away from the wall. Thus, another problem with DES is that the interface can be forced to move close to the wall, often as near as $y^+ \sim O(50-100)$, in which case RANS and LES regions co-exist even in fully attached flow. In such circumstances, it has been repeatedly observed, especially at high Reynolds numbers, that the high turbulent viscosity generated by the turbulence model in the inner region extends, as subgrid-scale viscosity, deeply into the outer LES region, caus-

ing severe damping in the resolved motion and a misrepresentation of the resolved structure as well as the time-mean properties. The DES method has recently been applied to the 3d-hill flow considered in the present paper by Persson et al. (2006) with some measure of success, in so far as the DES solutions were found to be materially closer to the measured data than those obtained with RANS.

A hybrid method allowing the RANS near-wall layer to be pre-defined and to be interfaced with the LES field across a prescribed boundary has recently been proposed by Temmerman et al. (2005). With such a method, one important issue is compatibility of turbulence conditions across the interface; another (related one) is the avoidance of 'double-counting' of turbulence effects – that is, the over-estimation of turbulence activity due to the combined effects of modelled and resolved turbulence. A general problem often observed with this type of hybrid scheme is an insufficient level of turbulence activity just beyond the interface, as a consequence of the near-wall RANS model misrepresenting the near-wall (streaky) structure and the fact that the turbulence in the LES region close to the interface is not sufficiently vigorous, because this region is subjected to wrong or distorted structural information at the interface. Several attempts have thus been made to inject synthetic turbulence into the interface in an effort to at least partially recover the influence of the small-scale structures lost by the application of the RANS model. Alternative approaches have been proposed by Piomelli et al. (2003), Davidson and Dahlstrom (2004) and Davidson and Billson (2006). While these measures have some beneficial effects, in terms of reducing mean-velocity anomalies, they do not and cannot cure most of the defects arising from the inevitable misrepresentation of the turbulence structure near the wall. They are also not practically usable in a general computational environment.

It is arguable that any near-wall approximation that circumvents a detailed resolution of the near-wall structure cannot be expected to return a physically correct spectral state and cannot, therefore, provide the correct 'boundary conditions' for the LES portion above the approximated near-wall layer. It can further be claimed, with some justification, that the most that a near-wall model can be expected to provide is a realistic representation of the wall-shear stress, and that this should be the only quantity that is fed into the LES procedure. This is the basis of a second group of approaches termed 'zonal schemes'. Like hybrid strategies, zonal schemes involve the application of a RANS model in the near-wall layer. However, they involve a more distinct division, both in terms of modelling and numerical treatment, between the near-wall layer and the outer LES region. Such schemes have been proposed and/or investigated in the context of LES by Balaras and Benocci (1994), Balaras et al. (1996), Cabot and Moin (1999), Wang and Moin (2002) and Tessicini et al. (2006). The same concepts underpin methodologies formulated by Ng et al. (2002) and Craft et al. (2004) for RANS computations. In all the above zonal schemes applied within LES, unsteady forms of the boundary-layer (or thin-shear-flow) equations are solved across an inner-layer of a prescribed thickness, which is covered with a fine wall-normal mesh, with a turbulence model providing the eddy viscosity. Computationally, this layer is partially decoupled from the LES region, in so far as the pressure field just outside the inner layer is imposed across the layer, i.e. the pressure is not computed in the layer. The principal information extracted from the RANS computation is the wall shear stress, which is fed into the LES solution as an unsteady boundary condition.

2. The two-layer zonal scheme

The objective of the zonal strategy is to provide the LES region with the wall-shear stress, extracted from a separate modelling process applied to the near-wall layer. Computationally, this layer is partially decoupled from the LES region, in so far as the pressure field just outside the inner layer is imposed across the layer, i.e. the pressure is not computed in the layer, which results in a major saving of computational resources. The principal information extracted from the RANS computation is the wall shear stress, which is fed into the LES solution as an unsteady boundary condition. A schematic of the method is shown in Fig. 2.

At solid boundaries, the LES equations are solved down to the wall, but over a relatively coarse near-wall mesh, with the wall-nearest node located, typically, at $y^+ = 30 - 50$. From this node to the wall, a refined mesh is embedded into the near-wall layer of LES cells, and the following simplified turbulent boundary-layer equations are solved:

$$\underbrace{\frac{\partial \rho \widetilde{U}_i}{\partial t} + \frac{\partial \rho \widetilde{U}_i \widetilde{U}_j}{\partial x_j} + \frac{\partial \widetilde{P}}{\partial x_i}}_{F_i} = \frac{\partial}{\partial y}\left[(\mu + \mu_t)\frac{\partial \widetilde{U}_i}{\partial y}\right] \quad i = 1, 3 \qquad (1)$$

where y denotes the direction normal to the wall and i identify the wall-parallel directions (1 and 3). The left-hand-side terms are collectively referred to as F_i.

In the present study, either none of the terms or only the pressure-gradient term in F_i has been included in the near-wall approximation. The effects of including the remaining terms are being investigated and will be reported in future accounts. Depending on the terms included, Eq. (1) can be solved algebraically or numerically, resulting in different

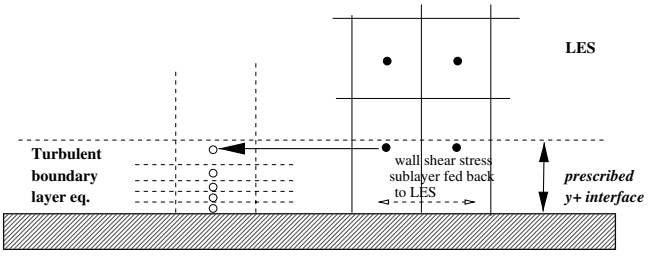

Fig. 2. Schematic of the two-layer zonal scheme.

degrees of simplification. The wall shear stress is then evaluated from the inner-layer solution.

The eddy viscosity μ_t is here obtained from a mixing-length model with near-wall damping, as done by Wang and Moin (2002):

$$\frac{\mu_t}{\mu} = \kappa y_w^+ (1 - e^{-y_w^+/A})^2 \quad (2)$$

The boundary conditions for Eq. (1) are given by the unsteady outer-layer solution at the first grid node outside the wall layer and the no-slip condition at $y = 0$. Since the friction velocity is required in Eq. (2) to determine y^+ (which depends, in turn, on the wall-shear stress given by Eq. (1)), an iterative procedure had to be implemented wherein μ_t is calculated from Eq. (2), followed by an integration of Eq. (1).

3. The computational LES framework

The computational method rests on a general multi-block, collocated-storage finite-volume scheme with non-orthogonal-mesh capabilities, allowing the mesh to be body-fitted. The scheme is second-order accurate in space, using central differencing for advection and diffusion. Time-marching is based on a fractional-step method, with the time derivative being discretized by a second-order backward-biased approximation. The flux terms are advanced explicitly using the Adams–Bashforth method. The provisional velocity field is then corrected via the pressure gradient by a projection onto a divergence-free velocity field. To this end, the pressure is computed as a solution to the pressure-Poisson problem by means of a three-dimensional V-cycle multigrid algorithm operating in conjunction with a successive-line over-relaxation scheme. The code is fully parallelized using MPI and was run on several multi-processor computers with up to 256 processors. The procedure is more fully described in Temmerman et al. (2003), and it has previously been used to investigate the turbulence physics in a variety of generic flows, among them attached wall jets (Dejoan and Leschziner, 2005) and the separated flow in a channel constricted by streamwise periodic, two-dimensional hills (Froehlich et al., 2005).

4. The simulated configurations

The three-dimensional circular hill, of height-to-base ratio of 4, is located on the bottom wall of a duct, as shown earlier in Fig. 1. The size of the computational domain is $16H \times 3.205H \times 11.67H$, with H being the hill height. The hill crest is $4H$ downstream of the inlet plane. One typical numerical mesh is shown in Fig. 3.

The inlet conditions required particularly careful attention in this flow, because the inlet boundary layer is thick, roughly 50% of the hill height. As indicated in Fig. 4, the mean flow was taken from a RANS simulation that accurately matched the experimental conditions (Wang et al., 2004). The spectral content was then generated separately by superposing onto the mean profile fluctuations taken from a separate precursor boundary-layer simulation, per-

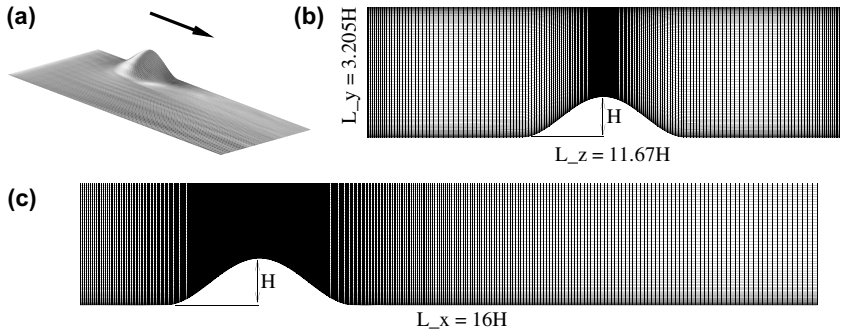

Fig. 3. Numerical grid: (a) perspective view of the computational domain (half); (b) grid in $y - z$ plane at $x = 0$ and (c) grid in $x - y$ plane at $z = 0$.

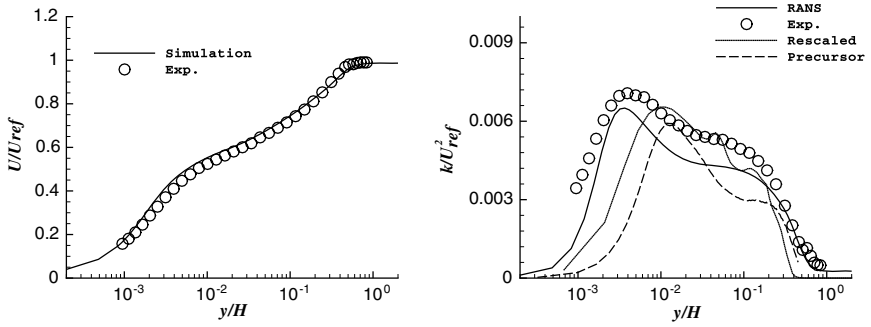

Fig. 4. The mean-velocity and turbulence-energy profiles at the inlet plane of the domain.

formed with a quasi-periodic recycling method, and rescaling the fluctuations by reference to the ratio of the friction-velocity values of the simulated boundary layer, at $Re_\theta = 1700$, and the actual boundary layer ahead of the hill, at $Re_\theta = 7000$. Although the fluctuations only roughly match the experimental conditions at the inlet – as can be seen from the turbulence-kinetic-energy profiles in Fig. 4 – specifying this reasonably realistic spectral representation proved to be decisively superior to simply using uncorrelated fluctuations (Li et al., 2005), even if the latter could be matched better to the experimental profile of the turbulence energy. In particular, the simulation returned the correct mean-flow evolution of the boundary layer downstream of the inlet, and the turbulence level was maintained at an approximately correct level, with a slight downstream increase in level taking place, in contrast to the precipitous decline observed when uncorrelated turbulence was prescribed. Also included is the result of a second precursor simulation, performed at the correct Reynolds number ($Re_\theta = 7000$), but over a grid that did not resolve the near-wall layer and relied on a log-law wall model to approximate this layer. As seen, the resulting turbulence-energy profile is not unambiguously superior to that arising from the rescaled lower-Reynolds-number simulation. It is arguable that a better approach would have been to add a duct portion upstream of the inlet and generate the inlet conditions, on the fly, by recycling the solution over this duct portion, subject to the assumption of streamwise quasi-periodicity, synchronously with the main LES solution over the hill domain. This approach requires neither rescaling nor interpolation in space and time to account for differences in mesh and time step between the precursor and the main simulations. However, this would have been substantially more resource intensive, and the outcome may well have been inferior in coarse-grid simulations in which the near-wall layer would have had to be approximated by whatever scheme was used in the hill domain. The latter point is illustrated by Fig. 4.

As the upper and side walls of the domain were far away from the hill, the spectral state of the boundary layers along these walls was ignored. Finally, at the exit, a convective, non-reflecting boundary condition was prescribed, which imposes zero change of velocity along the material time-space characteristic defined by the average duct velocity.

Table 1 summarizes the simulations performed for the three-dimensional hill. First, in order to provide reference results, additional to the experimental data, pure LES computations, without wall modelling, were performed on a mesh of 9.6-million-nodes with both the constant-coefficient, van-Driest-damped Smagorinsky model and its dynamic variant. In the former, damping is governed by the local y^+ in which the local wall shear stress is used. Spanwise averaging is used in conjunction with the latter model. It must be acknowledged that such averaging is questionable in the absence of spanwise homogeneity. However, tests with a time-averaged implementation yielded very similar results. Moreover, in the case of the coarse grids used herein in combination with the zonal near-wall approximation, the physical realism returned by the dynamic procedure is in question, in any event, because of the extreme coarseness of the test filter. Hence, any differences arising from spanwise, time-wise, or patchwise averaging are very likely to be of secondary importance.

Table 1
Grids, modelling practices and interface locations for the 3D-hill simulations

Case	Grid	SGS Model	y^+ of interface or near-wall-node location
Fine-grid LES	$448 \times 112 \times 192$	Dynamic	5–10
Fine-grid LES	$448 \times 112 \times 192$	Smagorinsky	5–10
Log-law WF	$192 \times 96 \times 192$	Dynamic	20–40
Two-layer zonal	$192 \times 96 \times 192$	Dynamic	20–40
Coarse-grid LES	$192 \times 96 \times 192$	Dynamic	20–40
Two-layer zonal	$192 \times 64 \times 128$	Dynamic	40–60
Two-layer zonal (with dp/dx_i)	$192 \times 96 \times 192$	Dynamic	20–40
Coarsest-grid LES	$192 \times 64 \times 128$	Dynamic	40–60

Despite the seemingly fine resolution achieved with the 9.6-million-node grid, these simulations are not, in fact, fully wall-resolving, as the y^+ values at the wall-nearest nodes upstream of the hill were of order 5. These simulations also display a non-negligible sensitivity to subgrid-scale modelling, which reinforces the observation that resolution is not as good as would be desired in a simulation that is beyond reproach. With wall models, the aspect ratio of the near-wall grid is (supposedly) no longer a crucial constraint for LES, and major savings in computational costs can be achieved by reducing the grid resolution in the streamwise and spanwise directions. This was realised with meshes of 3.5- and 1.5-million-nodes that were used with the zonal near-wall model. Zonal-scheme simulations on the finer mesh were performed with and without the pressure gradients included in the near-wall approximation. One further pure LES computation was undertaken with the coarsest mesh of 1.5-million-nodes with no-slip conditions imposed at the walls. Finally, a simulation was performed on the 3.5-million-node mesh with a conventional log-law-based wall function at the hill wall. In the discussion to follow, the 9.6-million, 3.5-million and 1.5-million node meshes are referred to as fine, coarse and coarsest, respectively.

5. Results and discussion

Prior to a consideration of results obtained with the near-wall approximations, attention is directed briefly to the pure LES solution on the 9.6-million-node mesh, some of which have already been reported by Tessicini et al.

(2005). As noted earlier, by reference to Table 1, the near-wall resolution in this simulation is insufficient, rendering it sensitive to sub-grid-scale modelling, especially very close to the wall, where the asymptotic variation of the sub-grid-scale viscosity and stresses can be very important. This sensitivity is illustrated in Fig. 5, which shows the mean velocity-vector fields across the hill centre-plane. With the Smagorinsky model, separation occurs too early and gives rise to a more extensive recirculation zone, which results in a slower pressure recovery in the wake following the separation and consequent differences in the flow fields downstream of reattachment. The dynamic model gives a shorter and thinner recirculation zone, in better agreement with the experimental observations.

Despite the broadly satisfactory results derived from the dynamic model, some caution is called for when assessing the physical fidelity of the results. As noted earlier, the use of the dynamic model poses uncertainties when it is applied on an under-resolving grid, because the near-wall variation of the Smagorinsky constant, following spatial averaging, is quite sensitive to the near-wall grid, and that grid is too coarse in the present LES computation. The fact that the dynamic model nevertheless performs better than the constant-coefficient variant is due to the former returning a better representation of the required wall-asymptotic variation of the Smagorinsky viscosity ($O(y^3)$). An estimate of the grid density required to yield a sufficiently well wall-resolved near-hill representation suggests the need for a grid of 30–50-million-nodes, an extremely expensive proposition in view of the modest Reynolds number.

Statistical results obtained with the wall-functions and zonal approximation are given in Figs. 6–15. In all these figures, the version of the zonal scheme used is that *without* the pressure gradient; separate comparisons between the versions that include and exclude the pressure gradient will be given at the end. These figures show, respectively, profiles of the pressure coefficient along the hill surface at the centre-plane, pressure contours on the hill surface, velocity-vector fields across the centre-plane, flow-topology maps on the leeward side of the hill, velocity profiles in the cross-flow plane at the downstream location $x/H = 3.63$, the wall-shear stress distribution and contours and profiles of turbulent kinetic energy at that same location at which experimental data are also available. Furthermore, some images of the instantaneous flow are given in Figs. 16 and 17, and these will support a discussion of some specific features of the unsteady motions.

Fig. 6(a) shows that, except for the coarsest-grid (1.5-million-nodes) pure LES, all simulations predict the pressure-coefficient distribution reasonably well. The magnified views provided in Fig. 6(b) and (c) reveal, in particular, that the inflexion in the C_p curves, associated with the weak separation on the leeward side of the hill, is well captured. The benefit of using wall models becomes especially evident in the case of extremely poor spatial resolution, on the 1.5-million-node mesh, where the use of no-slip conditions results in a grossly erroneous prediction of the separation process. In fact, as will be shown below, a fully attached flow is predicted, and an excessively fast pressure recovery after the hill crest is returned. In contrast, applying a wall

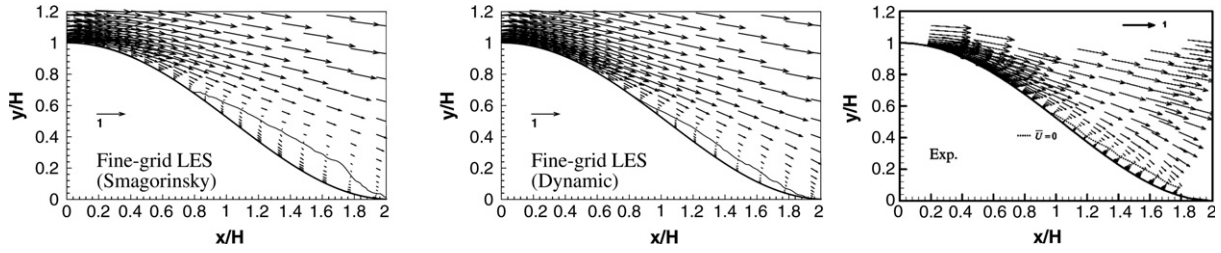

Fig. 5. Velocity fields across the centre-plane in the leeward portion of the hill – comparison between fine-grid LES solutions using different SGS models and the experiment.

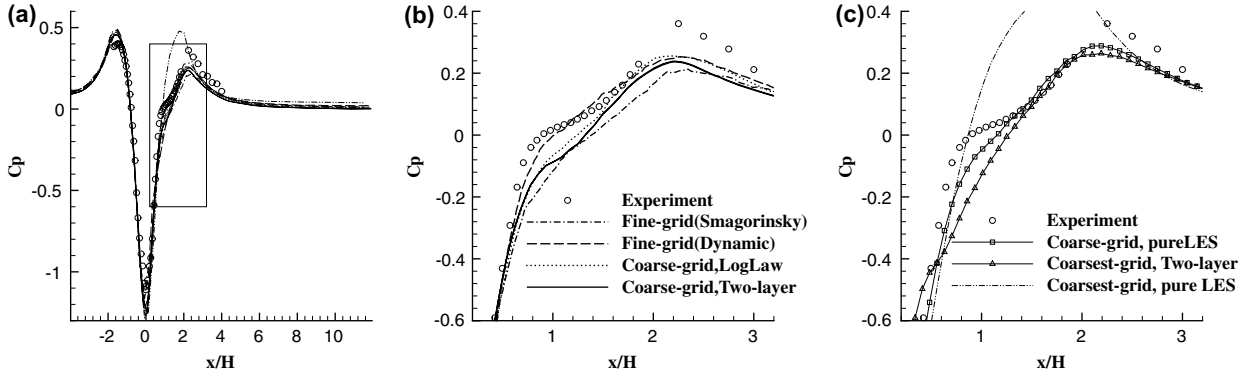

Fig. 6. Pressure coefficient along the hill surface at the centre-plane: (a) full view; (b) and (c) zoomed-in view around the region where separation occurs.

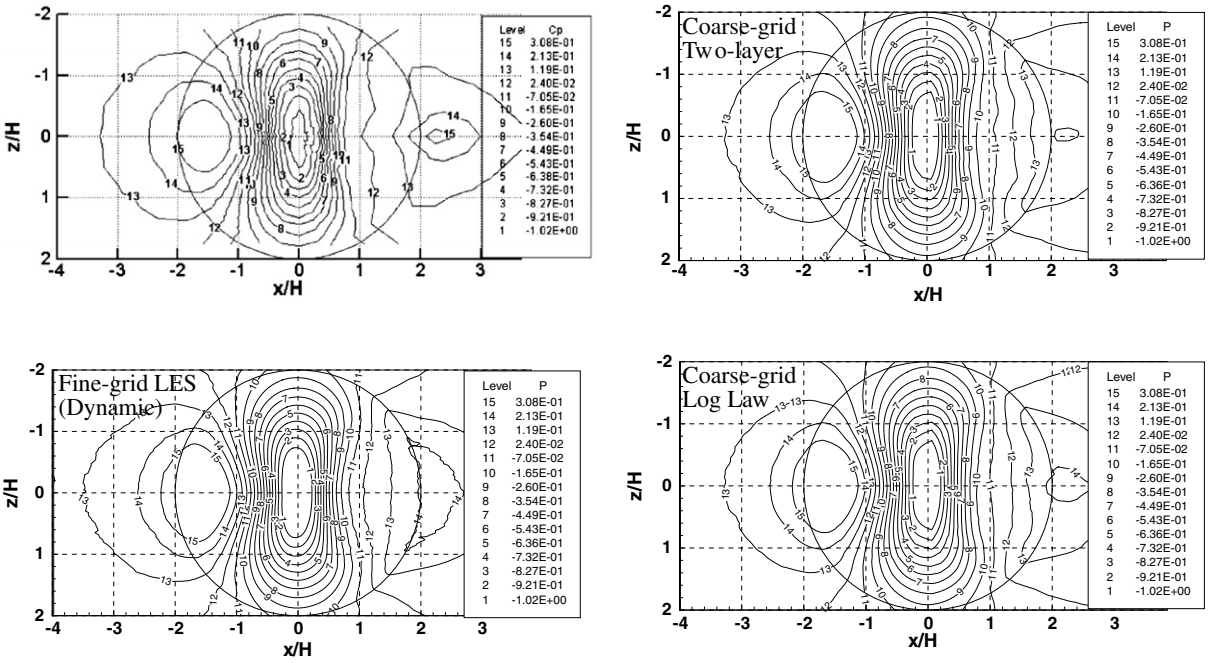

Fig. 7. Contours of the pressure coefficient on the hill. Comparison between the experiment, two coarse-grid simulations and one fine-grid simulation.

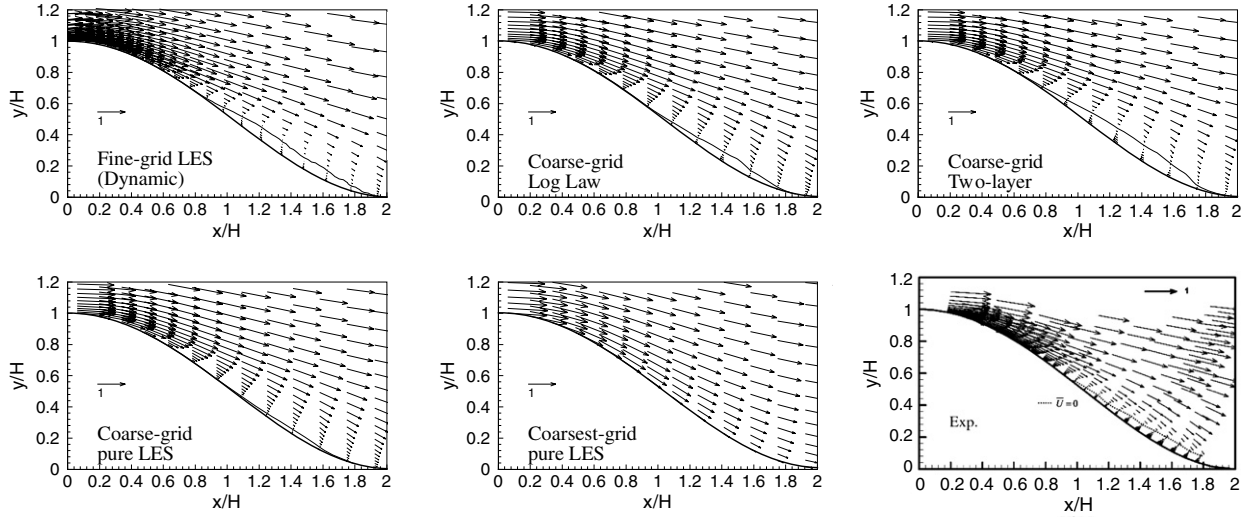

Fig. 8. Velocity field across the centre-plane in the leeward portion of the hill – comparison between pure LES solutions, wall-model solutions and the experiment. The zero-U-velocity lines indicate the recirculation zone.

model on the coarsest grid results in the resolution of the separation process and thus a reasonable representation of the pressure-recovery process.

Broader views of the pressure field are given in Fig. 7, which shows contour plots of C_p above the hill. The circles in these plots indicate the foot of the hill. The predicted fields, two derived from coarse-grid simulations and one from a fine-grid simulation, agree well with the experimental results of Simpson et al. (2002).

According to the experiment, the flow in the symmetry plane separates about 1 hill height ($x/H = 0.96$) after passing over the hill crest. The separation zone is very shallow, and the flow reattaches at the foot of the hill at $x/H = 2.0$. In the fine-grid simulations, as well as all simulations using wall models, the size and extent of the recirculation zone on the leeward side of the hill agree fairly well with the experimental results, as shown in Fig. 8. With poor spatial resolution and no-slip conditions, the recirculation zone predicted is either too small – as is the case for the coarse-grid LES on the 3.5-million-node mesh – or entirely absent – as is the case for the 1.5-million-node coarsest mesh.

Fig. 9 demonstrates that the simulations with the near-wall approximations also give a broadly faithful represen-

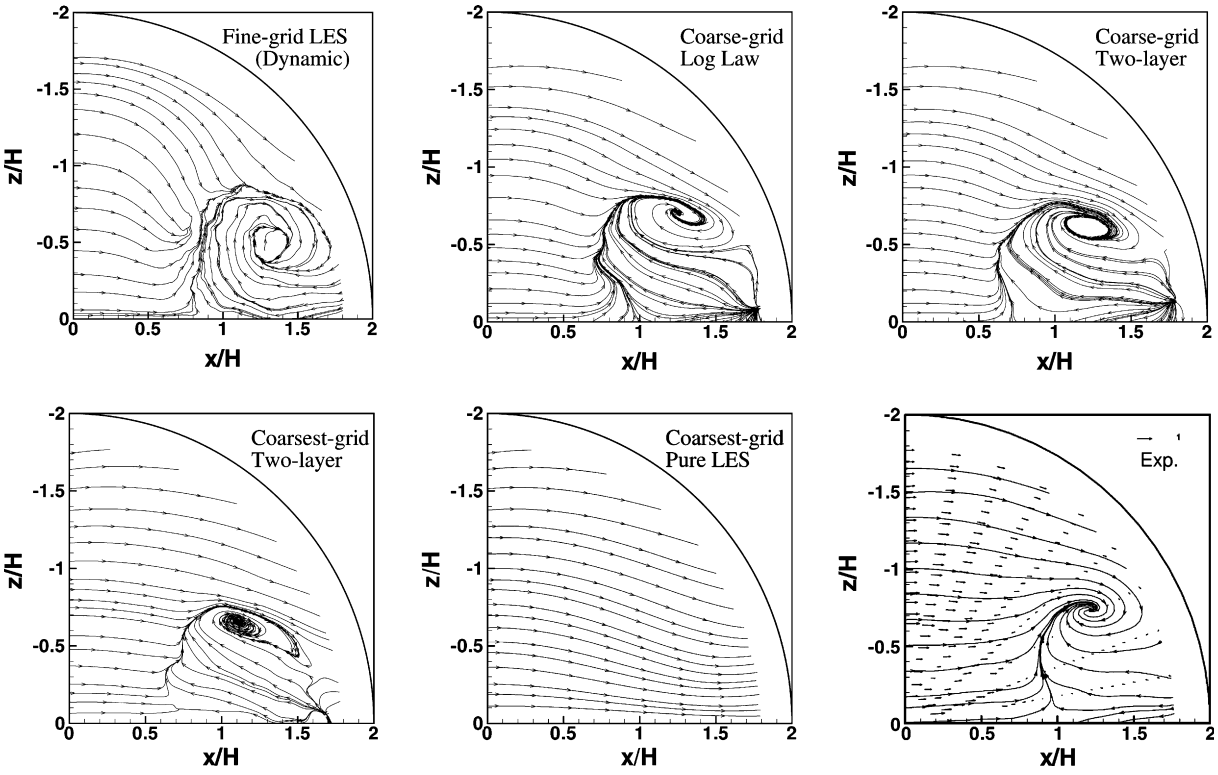

Fig. 9. Topology maps predicted by the wall models, relative to the pure LES and experiment.

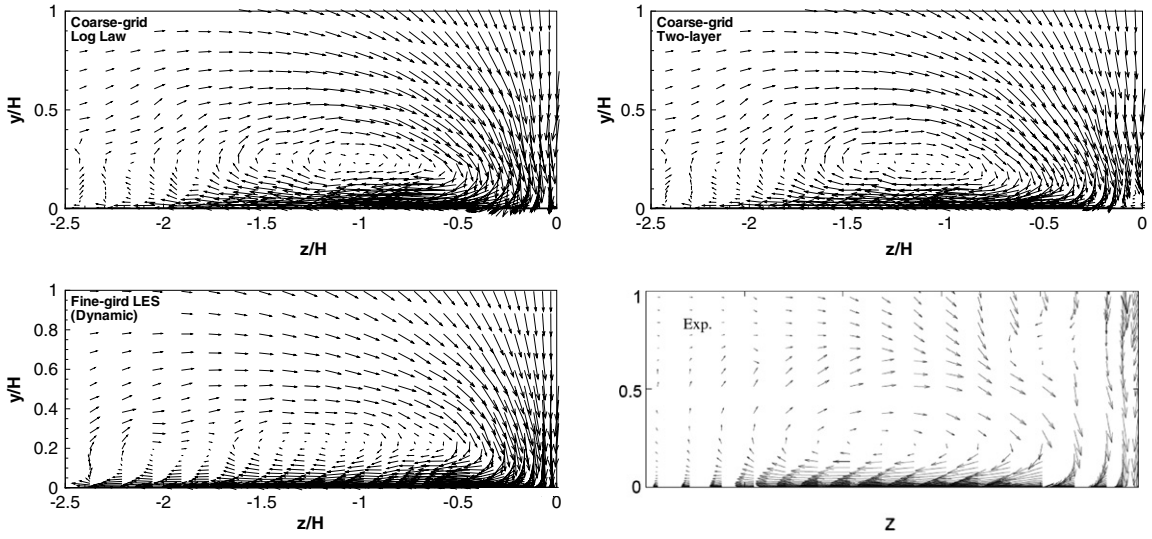

Fig. 10. Velocity vectors at $x/H = 3.63$ in the wake.

tation of the flow topology. The LDV experiment by Byun and Simpson (2005) reveal the presence of a pair of counter-rotating vortices detaching from the leeward side of the hill and centred at approximately $x/H = 1.2$ and $z/H = \pm 0.7$. This feature is well captured by the simulations, especially by those involving wall models. With the combination of the coarsest-grid and the no-slip conditions, the topology is seen to be characterized by streaklines identifying a fully attached flow. This is not surprising, as the wall-normal height of the cells closest to the wall are comparable with the thickness of the separation zone. However, with the zonal model, a realistic representation of the wall shear stress is returned, and the correct vortical structure is recovered.

Downstream of the hill, in the wake region, one major flow feature is a pair of counter-rotating streamwise vortices, shown in Fig. 10. These originate from the vorticity in the boundary layer upstream of the hill and that generated

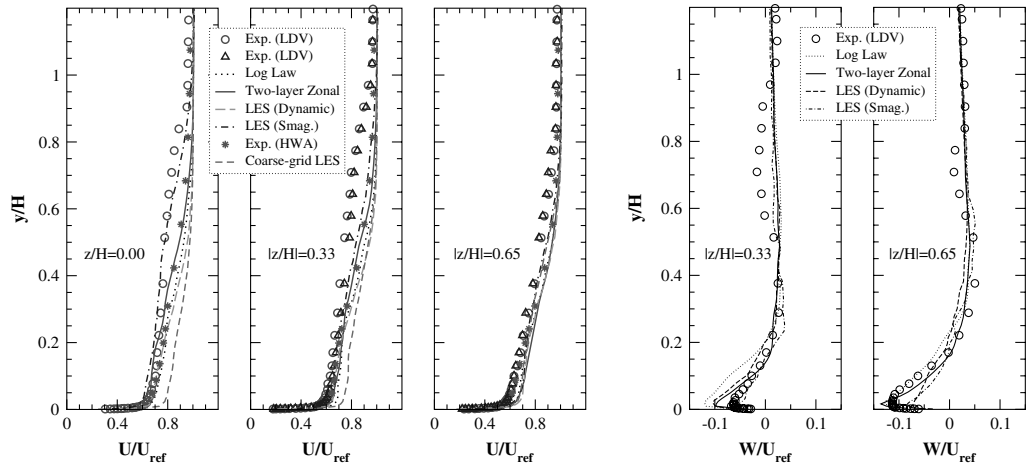

Fig. 11. Mean streamwise- and spanwise-velocity profiles at various spanwise locations on the downstream plane $x/H = 3.63$.

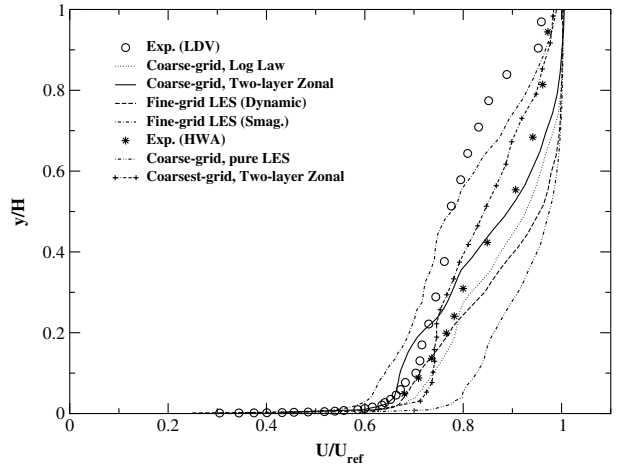

Fig. 12. Magnified view of the mean streamwise velocity distribution at $z/H = 0$ on the downstream plane $x/H = 3.63$.

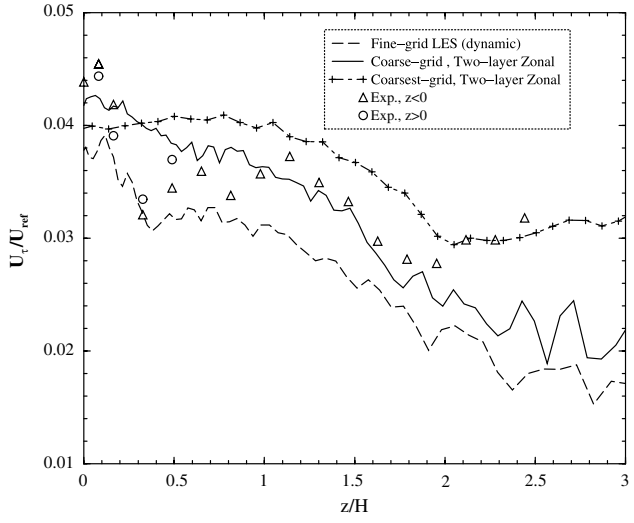

Fig. 13. Variation of the fricton velocity at $x/H = 3.63$.

on the hill itself. The simulations are in fairly close agreement with the experimental data. One discrepancy arises, however, around the location $y/H = 0.7$ and $z/H = \pm 0.4$, where the LDV measurements clearly indicate the existence of secondary vortices. Neither the simulations performed by the present authors, nor the CFD studies performed by other researchers, i.e. Benhamadouche et al. (2005), predict these secondary vortices. A Proper Orthogonal Decomposition (POD) (Berkooz et al., 1993), discussed later, suggests that the vorticity shed from the focus on the hill surface is propagated approximately to the location at which the measurements return the secondary vortex. However, in the simulation, this vortex is not visible in the time-averaged transverse-velocity field. Hence, if the measurements are correct (and there are some significant doubts about this region, for reasons explained below), it must be concluded that lack of resolution prevents the secondary vortex from being visibly captured; the vorticity may be present, but may be smeared to an extend preventing the vortical feature from becoming evident.

To examine the wake statistics in detail, streamwise- and spanwise-velocity profiles at various spanwise locations on the plane $x/H = 3.63$ are shown in Fig. 11. Three sets of experimental data are included: two obtained with LDV, on either side of the centre-plane, and the third obtained by means of HWA in the same facility by Ma and Simpson (2005). A magnified view of the streamwise velocity on the centre plane, providing a greater degree of differentiation, is given in Fig. 12. Consistent with the earlier results, the excessively large separation zone, returned by the fine-grid LES with the Smagorinsky model, goes hand-in-hand with a too slow recovery of the flow in the wake, so that the near-wall streamwise velocity is under-predicted by that simulation. On the other hand, when a simulation fails to capture the separation (as is the case with the coarse grid and no-slip conditions), or when the reattachment occurs too early at the foot of the hill, the flow recovers at an excessive rate, and the streamwise velocity is over-predicted. All the computations performed either with the two-layer zonal model or with the log-law wall function generally give much better results than those performed with the no-slip condition.

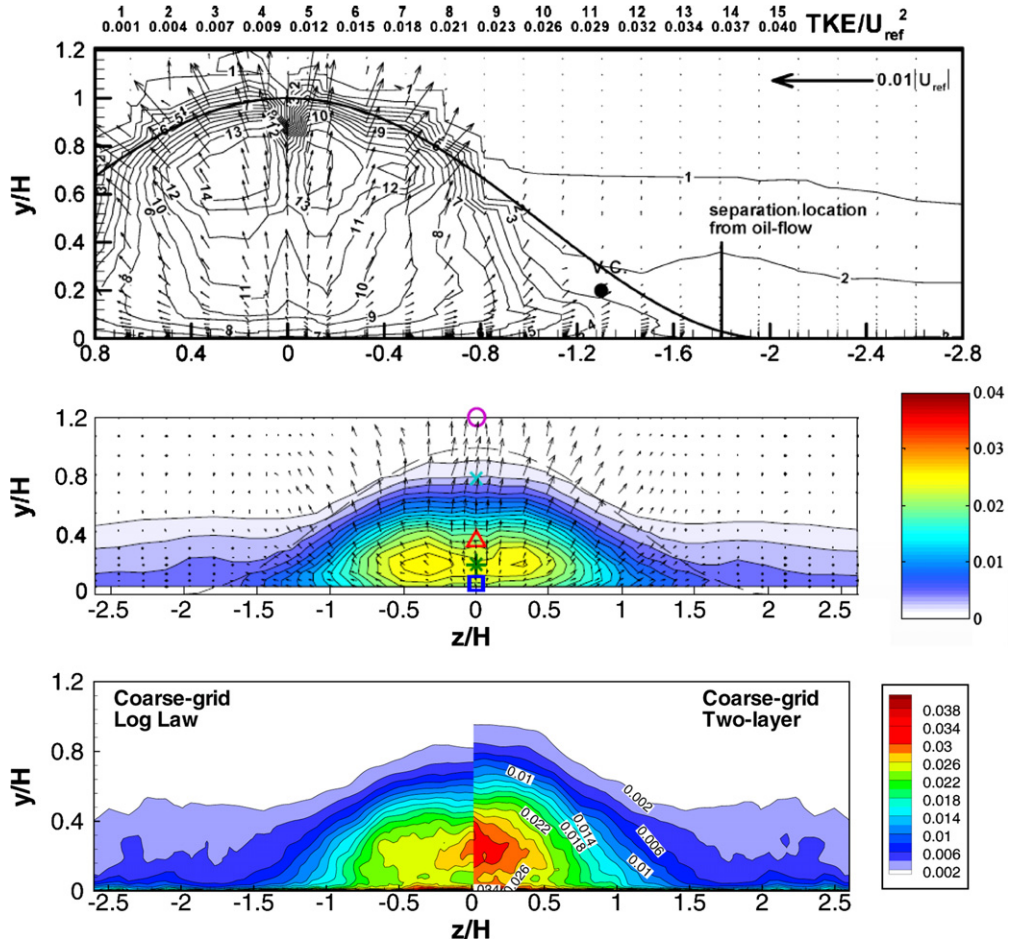

Fig. 14. Turbulent kinetic-energy distribution at $x/H = 3.63$. Top: LDV measurement; middle: HWA measurement; bottom: simulations.

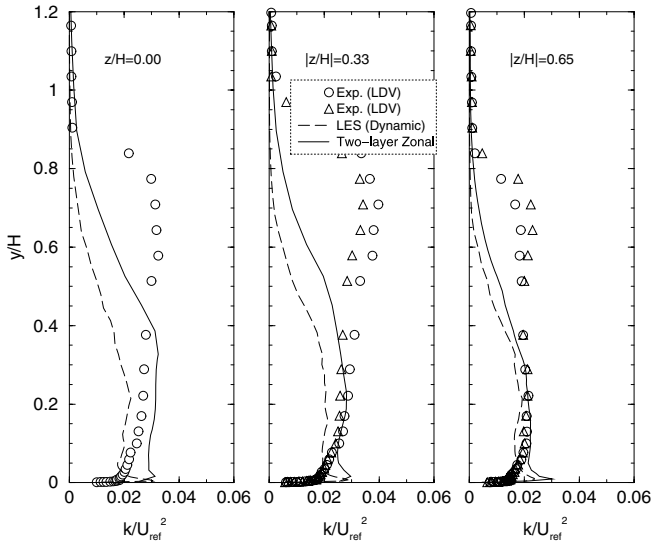

Fig. 15. Turbulent kinetic-energy profiles at various spanwise locations on the downstream plane $x/H = 3.63$.

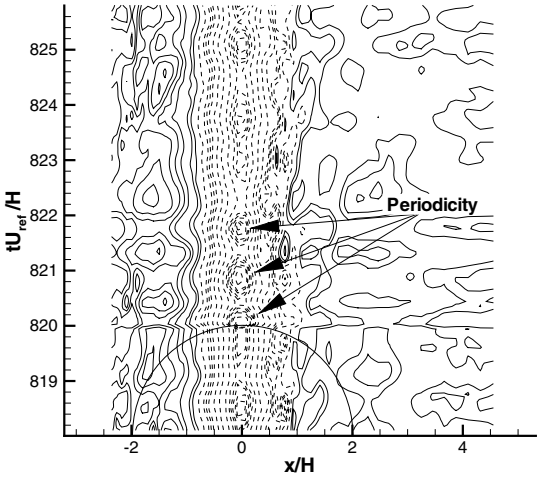

Fig. 16. Temporal evolution of the pressure field above the hill crest on the centre plane.

In the region far away from the wall, beyond $y/H = 0.4$, the predicted velocity profiles are noticeably different from the experimental LDV data, while they agree closely with the HWA measurements. The differences between the two sets of experimental data are obviously disconcerting. The present authors are only able to report that the experimental investigators have expressed their view, in a private communication, that the LDV data are erroneous in regions remote from the wall, due to seeding problems, and that the HWA data are to be preferred.

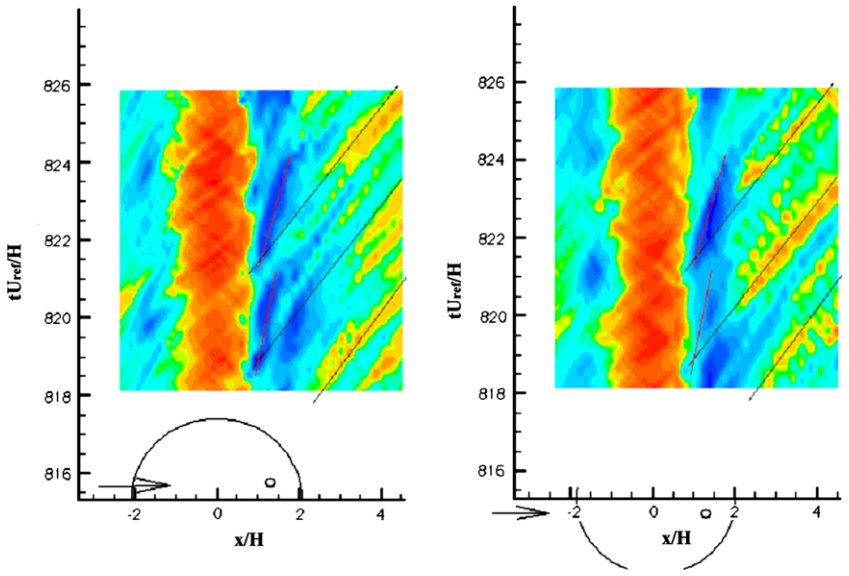

Fig. 17. Temporal evolution of vortical structures above the hill crest, indicating that the time-evolving flow is symmetric.

Fig. 13 shows the z-wise distribution of the friction velocity on the lower wall at $x/H = 3.63$ in the wake, obtained upon time-averaging the instantaneous wall shear stress that is returned by the wall model through the inner-layer velocity profiles. Comparisons are made among the fine-grid result, two zonal-model results and the experiment. The wall-shear stress is the principal output sought from the wall model, and it is therefore of particular interest in the context of this study. It is also an especially sensitive indicator of the near-wall conditions, and is a variable that displays, more prominently than other mean-flow quantities, a slow statistical convergence. This is the reason for the rather 'noisy' appearance of the distributions in Fig. 13, also linked to the undulations in the near-wall streamwise velocity seen in Fig. 12. While longer integration times than those adopted would have led to smoother variations, especially for the 3.5- and 9.6-million-node simulations, the attendant costs for the finer were deemed to be excessive relative to anticipated benefits.

As seen, there is a fair agreement among the skin-frictions distributions arising from the simulations and also with the experimental data. Curiously, the largest differences arise beyond the base of the hill, $z/H > 2$, i.e. outside the most complex flow region recovering from separation. With a spanwise grid-expansion ratio being only 1.027, the cell aspect ratio at $z/H = 2$ is not much higher than in the central region, reaching only 12.6 at $z/H = 4$. Hence, the resolution in the outer area is not seriously inferior to that in the central duct portion. On the assumption that the experimental data are correct, it is conceivable that the discrepancies reflect a failure of the simulation to resolve the effects of the (relatively weak) legs of the horseshoe vortex on either side of the hill, associated with the vorticity in the upstream boundary layer. The experiments (see Fig. 14, discussed later) show a bulge-like region of elevated turbulence energy close to the wall around $z/H = 2$, while the simulation only hints at this feature. As near-wall turbulence tends to go hand-in-hand with the wall-shear stress in boundary layers, the experimental trends in this region seem credible. Another possible source for the differences is that the near-wall turbulence state is perhaps more sensitive than in other regions to the ability of the simulation to resolve the slowly evolving boundary-layer structure and its readjustment from the approximate state prescribed at the inlet. Close to the centre-plane, the fine-grid simulation goes some way towards capturing the distinct peak of the wall-shear stress, presumably reflecting the high turbulence activity originating from the reattachment area upstream and convected downstream. This feature is not resolved by the zonal-model simulations, because turbulence transport is not accounted for in the near-wall region, and there is no mechanism for sensitising the shear stress to the turbulence level above the near-wall layer.

Fig. 14 shows contours of the turbulent kinetic energy, normalised by the square of the free-stream velocity, on the same cross-wake plane considered above. Included in the figures are numerical results obtained from the 3.5-million-node simulations performed with the log-law wall function and the two-layer zonal scheme, and these are compared to two sets of experimental results, one obtained by LDV (top plot) and the other with HWA (middle plot).[1] Here again, disconcertingly large differences between the two sets of experimental data are evident, and it is recalled that the experimental investigators attribute this to seeding-related errors in the LDV measurements. The LDV data show the maximum of turbulence energy to occur around $y/H = 0.7 - 0.8$ (see also Fig. 15), while the maxi-

[1] The arrows superimposed on the contours do not identify transverse motion, but represent diffusive transport fluxes of turbulence energy, associated with triple correlations.

mum returned by the HWA measurements is at around $y/H = 0.3$. More generally, the LDV data imply that the region of high turbulence activity is substantially further from the lower wall, relative to that suggest by the HWA results. The computations return a broadly satisfactory agreement with the HWA data, but not the LDV field. With the zonal model, the lateral extent the turbulent wake is better predicted, but the central portion of the wake is more highly turbulent than the measured level – roughly 0.035 as compared to 0.025). Fig. 15 provides a comparison of computed and measured profiles of turbulence energy at three spanwise locations, all within the streamwise plane $x/H = 3.63$ – that is, the same plane to which Fig. 10 relates. The measured profiles suggest two principal regions of high turbulence activity: one close to the wall, at around $y/H = 0.2$, and the other much higher, at around $y/H = 0.8$, the latter being consistent with the top contour plot in Fig. 10 which arises from the LDV measurements. The maximum at the higher elevation is rather surprising on several grounds. First, the velocity profiles, Fig. 11, show that the shear strain at this elevation is rather weak – certainly too weak to explain why local shear-induced generation would cause the turbulence level to be above that in the wake of the separated region in which turbulence is strongly elevated by convection of turbulence from upstream. Second, the field of transverse motion, Fig. 10, suggests the presence of rather weak convective transport of turbulence from the lower-wall layer towards the upper part – and in any event, the simulation reproduces (if not over-estimates) this motion that would be the cause of this transport. Third, Fig. 8 suggests that the motion in the centre-plane, in the leeward side, is predominantly downwards, and this process is also indicated by the diverging streaklines around the centre-line behind the hill, not included herein. This downward motion would thus tend to transport turbulence from upper regions towards the wall, rather than supply the upper region with highly turbulent fluid. A feature that might be linked to the elevated turbulence energy at around $y/H = 0.7$ is the secondary vortex found at the location $z/H = 0.4$, $y/H = 0.7$ by the LDV measurement in the transverse velocity field shown in Fig. 10. It has been conjectured in an earlier part of this discussion – partly on the basis of a POD of the velocity field, discussed later – that this vortex reflects the ejection of vortical fluid from the recirculation region away from the leeward side of the hill. This ejection, which must be assumed to be present, is evidently not resolved by the simulations, or is too diffuse to be brought out. Whether and how the two features are linked is not possible to be determined from the data so far available.

While the statistical results of the flow are evidently in fairly good agreement with the experiments, a closer examination of the turbulent structures is desirable to shed light on some of the detailed physics and dynamics of the flow. One particularly influential unsteady process is the shedding (or ejection) of large-scale vortical structures from the leeward side of the hill and their interactions with the downstream boundary layer. Thus, Byun and Simpson (2005) have observed very-low-frequency, large-amplitude spanwise 'meandering' motion of the shed vortex structures. Efforts to visualize, identify and analyze these coherent structures from the simulations are far from straightforward, due to the complexity of the flow. Conventional methods for detecting coherent vortices, such as the Q and λ_2 criteria, do not work effectively for this flow. Also, the subtle nature and the low frequency of any periodic process make its detection a difficult task. In the present paper, we confine ourselves to giving a few observations on some unsteady motions in the flow. A detailed study on this subject will be reported elsewhere.

Fig. 16 shows time-space plots of the hill-surface pressure along the line $z/H = 0$, above the hill crest. The figure suggests the existence of a weak form of 'shedding'. Thus, an almost periodic variation of the pressure field is observed, with a non-dimensional frequency $fH/U_{\mathrm{ref}} \approx 0.83$. Fig. 17 shows the temporal evolution of the near-wall streamwise velocity at $z/H = \pm 0.4$ at either side of the hill. This reveals a temporal pattern consistent with that shown in Fig. 16, and it also indicates that the shedding is nearly symmetrical, rather than alternating. Clearly, this type of periodicity is unrelated to conventional vortex shedding behind bluff bodies, and their origin is a subject of ongoing studies.

Although the vortical structures shed from the hill are obscured by a broad range of smaller-scale motions and do not reveal themselves in conventional visualisation or in the statistical results, they can be detected and visualized through the reconstruction of the most energetic modes of motion obtained by POD. At the time of writing, these studies are still incomplete, but Fig. 18 gives a flavour of the outcome of a POD analysis based on 700 samples covering a period of 160 time units (U_{ref}/H). The analysis includes the lowest four POD modes (in addition to mode 0, representing the mean flow) extracted from the data of the simulation on the 3.5-million-node mesh. The figure shows the cores of vortical structures, forming a family of Ω-shaped vorticity lines, that originate from the focal points on the hill (included in the upper-left inset), are ejected into the wake and evolve in space in a manner similar to hairpin vortices. The upper-right inset shows a pair of counter-rotating structures through streaklines constructed with the low-order POD representation of the transverse velocity in the downstream plane $x/H = 2.2$. These results support the earlier statement that the nearly periodic shedding process is symmetric.

All the results presented so far for the zonal two-layer model were obtained with the pressure gradient omitted from the solution of the wall-layer Eq. (1). Clearly, a more general formulation would include the pressure gradient and also the convective terms. The latter extension is the subject of ongoing work. Here, the consequences of including the pressure gradient are briefly considered. Thus, Fig. 19 compares the topology on the leeward portion of the hill surface predicted without and with the pressure gra-

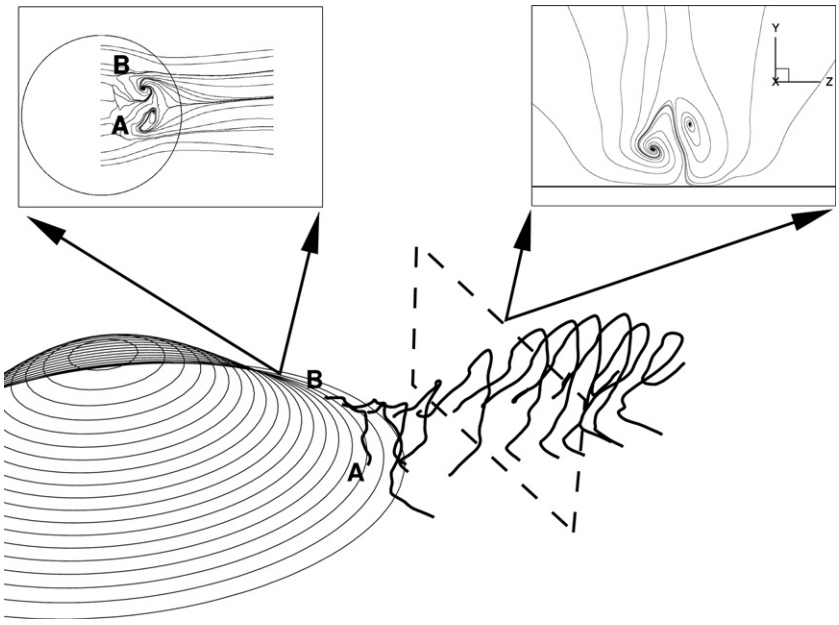

Fig. 18. Flow field reconstructed using the five most energetic POD modes based on the coarse-grid LES. Upper left: streaklines at 0.01 H above the hill surface. Upper right: streaklines at $x/H = 2.2$.

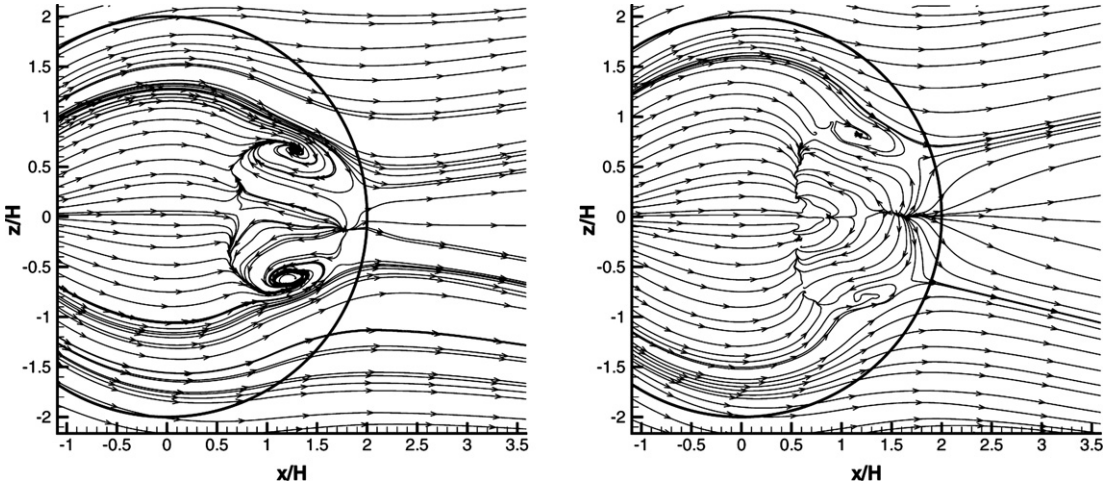

Fig. 19. The flow topology predicted by the two-layer zonal model without (left) and with (right) the pressure-gradient term.

dient in the near-wall model. The two simulations are seen to produce similar global features, with slightly different structures in the vicinity of the foci and the reattachment point. Significantly, the inclusion of the pressure gradient leads to a slight shift of the separation line towards the hill crest. This is the expected qualitative response, for the adverse pressure gradient in the separation region results in a reduction in the predicted wall shear stress returned by the extended formulation. Other than these differences, respective flow statistics derived from the two simulations, especially those downstream of the hill in the wake area, have been found to be close, and these comparisons are not included herein.

It is appropriate to finally point out that the effects of modifying the wall model, detrimental or beneficial, cannot easily be identified or isolated without the ambiguity that arises from other numerical issues. In particular, all simulations are under-resolved, and the role of the subgrid-scale model in the under-resolved environment has already been pointed out. This is not only a problem with the present extension, but also with that involving the inclusion of the convection terms in Eq. (1). The latter makes the model non-linear, non-local and thus much more expensive to solve.

6. Conclusions

The emphasis of this study has been on the ability of LES to reproduce the challenging process of three-dimensional separation from a gently curved surface. This is,

arguably, a very important generic configuration in the context of off-design external aerodynamics. Received wisdom is that any flow of the type examined is highly sensitive to the details of the description upstream of the separated region – i.e. the structure of the boundary layer and the accuracy with which the near-wall layer is resolved.

In the present study, simulations have been performed with grids which, without doubt, do not fully resolve the flow, in so far as a not insignificant proportion of the turbulence activity is not resolved, but is filtered and/or represented by the subgrid-scale model, even with the finest grid of close to 10-million-nodes. Moreover, the near-wall region was modelled with a rather crude approximation, which may be regarded as a variation of log-law-based wall functions. Yet, the results obtained are pleasingly close to the experimental observations – certainly much closer than achieved with RANS models.

As the predictive quality depends significantly on the resolution of the LES grid, the performance of the subgrid-scale model, especially in the ill-resolved near-wall region, and the spectral description of the inflow, it is difficult to unambiguously isolate and quantify the role of the near-wall model in the favourable outcome of the simulations. However, it is reasonably clear that prescribing, simplistically, a no-slip condition at the wall in coarse-grid simulations, and extracting the shear stress from the predicted near-wall velocity gradient is decidedly inferior to using even simple near-wall models that return reasonable values for the wall-shear stress. This is reflected by the outcome of simulation with the coarsest grid of 1.5-million-nodes, in which case the use of a no-slip condition resulted in the separation being entirely missed. With the near-wall models examined herein, most flow properties are fairly well – indeed, surprisingly well – predicted. In particular, the extent of the separated zone on the leeward side of the hill, the surface-pressure field and the flow topology are well reproduced, and the wake structure is also broadly correct. Inclusion of the pressure gradient in the near-wall model has not been found to have a decisive effect on the predictive accuracy.

A specific experimentally-observed feature that has not been resolved is a pair of small secondary vortices lying next to the much larger and dominant primary vortices associated with the interaction of the upstream boundary layer with the hill. These vortices could be the 'foot prints' of the vortical separation originating from the focal points on the leeward side of the hill. A POD study lends support to this supposition, but the strength of the secondary vortices is evidently too low, or the vorticity too diffuse to be visible in the time-mean transverse-velocity field. On the other hand, there are justifiable doubts about the validity of the LDV data in the region containing the measured secondary vortices.

A limited examination of unsteady fields revealed an intriguing periodicity in the pressure and velocity fields downstream of the hill crest. This does not seem to be related in any obvious way to conventional shedding: the frequency of the periodic features does not agree with that of shedding behind bluff bodies, and there is no alternate motion suggestive of conventional vortex shedding. The results of the POD also indicate that the shedding is symmetric.

Acknowledgements

This work was undertaken, in part, within the DESider project (Detached Eddy Simulation for Industrial Aerodynamics). The project is funded by the European Union and administrated by the CEC, Research Directorate-General, Growth Programme, under Contract No. AST3-CT-2003-502842.

N. Li and M.A. Leschziner gratefully acknowledge the financial support provided by BAE Systems and EPSRC through the DARP project "Highly Swept Leading Edge Separation".

References

Balaras, E., Benocci, C., 1994. Subgrid-scale models in finite difference simulations of complex wall bounded flows. Applications of Direct and Large Eddy Simulation, AGARD, 2-1–2-6.

Balaras, E., Benocci, C., Piomelli, U., 1996. Two-layer approximate boundary conditions for large-eddy simulations. AIAA Journal 34 (6), 1111–1119.

Benhamadouche S., Uribe J., Jarrin N., Laurence D., 2005. In: 4th International Symposium on Turbulence and Shear Flow Phenomena (TSFP4), Williamsburg, pp. 325–330.

Berkooz, G., Holmes, P., Lumley, J.L., 1993. The proper orthogonal decomposition in the analysis of turbulent flows. Annual Review of Fluid Mechanics 25 (1), 539–575.

Byun, G., Simpson, R.L., 2005. Structure of three-dimensional separated flow on an axisymmetric bump. AIAA Paper, 2005-0113.

Cabot, W., Moin, P., 1999. Approximate wall boundary conditions in the large eddy simulation of high Reynolds number flow. Flow, Turbulence and Combustion 63, 269–291.

Chaouat, B., Schiestel, R., 2005. A new subgrid-scale stress transport model and its application to LES of evolving complex turbulent flows. In: 4th Int. Symp. on Turbulence and Shear Flow Phenomena (TSFP4), Williamsburg, pp. 1061–1066.

Craft, T.J., Gant, S.E., Iacovides, H., Launder, B.E., 2004. A new wall function strategy for complex turbulent flows. Numerical Heat Transfer, Part B: Fundamentals 45 (4), 301–318.

Davidson, L., Billson, M., 2006. Hybrid LES-RANS using synthesized turbulent fluctuations for forcing in the interface region. International Journal of Heat and Fluid Flow 27 (6), 1028–1042.

Davidson, L., Dahlstrom, S., 2004. Hybrid LES-RANS: an approach to make LES applicable at high Reynolds number. In: de Vahl Davis, G., Leonardi, E. (Eds.) Procs CHT-04 Advances in Computational Heat Transfer III. Norway.

Deardorff, J.W., 1970. A numerical study of three-dimensional turbulent channel flow at large Reynolds numbers. Journal of Fluid Mechanics 41, 453–480.

Dejoan, A., Leschziner, M.A., 2005. Large eddy simulation of a plane turbulent wall jet. Physics of Fluids 17 (2), paper 025102.

Froehlich, J., Mellen, C., Rodi, W., Temmerman, L., Leschziner, M.A., 2005. Highly resolved large eddy simulation of separated flow in a channel with streamwise periodic constrictions. Journal of Fluid Mechanics 526, 19–66.

Helman, J.L., Hesselink, L., 1990. Surface representations of two- and three-dimensional fluid flow topology. In: Proceedings of the 1st

conference on Visualization '90. IEEE Computer Society Press, pp. 6–13.

Hoffmann, G., Benocci, C., 1995. Approximate wall boundary conditions for large-eddy simulations. In: Benzi, R. (Ed.), Advance in Turbulence V. pp. 222–228.

Li, N., Wang, C., Avdis, A., Leschziner, M.A., Temmerman, L., 2005. Large eddy simulation of separation from a three-dimensional hill versus second-moment-closure RANS modelling. In: 4th Int. Symp. on Turbulence and Shear Flow Phenomena (TSFP4), Williamsburg, pp. 331–336.

Ma, R., Simpson, R.L., 2005. Characterization of turbulent flow downstream of a three-dimensional axisymmetric bump. In; 4th Int. Symp. on Turbulence and Shear Flow Phenomena (TSFP4), Williamsburg, pp. 1171–1176.

Ng, E.Y.K., Tan, H.Y., Lim, H.N., Choi, D., 2002. Near-wall function for turbulence closure models. Computational Mechanics 29, 178–181.

Perry, A.E., Chong, M.S., 1987. A description of eddying motions and flow patterns using critical-point concepts. Ann. Rev. Fluid Mech. 19, 125–155.

Persson, T., Liefvendahl, M., Bensow, R.E., Fureby, C., 2006. Numerical investigation of the flow over an axisymmetric hill using LES, DES and RANS. Journal of Turbulence 7 (4), 1–17.

Piomelli, U., Balaras, E., Pasinato, H., Squires, K.D., Spalart, P.R., 2003. The inner-outer layer interface in large-eddy simulations with wall-layer models. International Journal of Heat and Fluid Flow 24 (4), 538–550.

Schiestel, R., Dejoan, A., 2005. Towards a new partially integrated transport model for coarse grid and unsteady turbulent flow simulations. Theoretical and Computational Fluid Dynamics 18 (6), 443–468.

Schumann, U., 1975. Subgrid scale model for finite difference simulations of turbulent flows in plane channels and annuli. Journal of Comparative Physiology 18, 376–404.

Simpson, R.L., Long, C.H., Byun, G., 2002. Study of vortical separation from an axisymmetric hill. International Journal of Heat and Fluid Flow 23 (5), 582–591.

Spalart, P.R., Jou, W.-H., Strelets, M., Allmaras, S.R., 1997. Comments on the feasibility of LES for wings and on the hybrid RANS/LES approach. In: Advances in DNS/LES, 1st AFOSR International Conference on DNS/LES, Greyden Press, pp. 137–148.

Temmerman, L., Leschziner, M.A., Hanjalić, K., 2002. A-priori studies of a near-wall RANS model within a hybrid LES/RANS scheme. In: Rodi, W., Fueyo, N. (Eds.), Engineering Turbulence Modelling and Experiments. Elsevier, pp. 317–326.

Temmerman, L., Leschziner, M.A., Mellen, C.P., Frohlich, J., 2003. Investigation of wall-function approximations and subgrid-scale models in large eddy simulation of separated flow in a channel with streamwise periodic constrictions. International Journal of Heat and Fluid Flow 24 (2), 157–180.

Temmerman, L., Hadziablić, M., Leschziner, M.A., Hanjalić, K., 2005. A hybrid two-layer URANS-LES approach for large eddy simulation at high Re. International Journal of Heat and Fluid Flow 26 (2), 173–190.

Tessicini, F., Li, N., Leschziner, M.A., 2005. Zonal LES/RANS modelling of separated flow around a three-dimensional hill. ERCOFTAC Workshop Direct and Large-Eddy Simulation-6, Poitiers.

Tessicini, F., Temmerman, L., Leschziner, M.A., 2006. Approximate near-wall treatments based on zonal and hybrid RANS-LES methods for LES at high Reynolds numbers. International Journal of Heat and Fluid Flow 27 (5), 789–799.

Wang, M., Moin, P., 2002. Dynamic wall modelling for large-eddy simulation of complex turbulent flows. Physics of Fluids 14 (7), 2043–2051.

Wang, C., Jang, Y.J., Leschziner, M.A., 2004. Modelling 2 and 3-dimensional separation from curved surfaces with anisotropic-resolving turbulence closures. International Journal of Heat and Fluid Flow 25, 499–512.

Werner, H., Wengle, H., 1991. Large-eddy simulation of turbulent flow over and around a cube in a plate channel. 8th Symposium on Turbulent Shear Flows, pp. 155–168.